Retrieval of Slant Water Vapor Path and Slant Liquid Water from Microwave Radiometer Measurements during the DYNAMO Experiment

Swaroop Sahoo, Xavier Bosch-Lluis, Steven C. Reising, *Senior Member, IEEE*, Scott M. Ellis, Jothiram Vivekanandan, *Senior Member, IEEE*, and Paquita Zuidema

***Abstract*—Observations during the Dynamics of the Madden–Julian Oscillation (DYNAMO) experiment focused on sensing atmospheric parameters, including vertical moisture profiles, cloud structure, precipitation processes, and planetary boundary layer properties, all of which are important for understanding and modeling the Madden–Julian Oscillation (MJO). These observations were performed using a variety of *in-situ* and remote sensors, including the S-band polarimetric and Ka-band (S-PolKa) radar, deployed by the National Center for Atmospheric Research (NCAR), and a colocated University of Miami microwave radiometer (UM-radiometer) operating at 23.8 and 30.0 GHz. These instruments sampled approximately the same volumes of the atmosphere at a variety of azimuth and elevation angles. The principal goal of this study is to develop a new retrieval strategy to estimate slant water vapor path (SWP) and slant liquid water (SLW) using UM-radiometer measurements from zenith to low elevation angles at a variety of azimuth angles. Retrievals of SWP along the radar signal path help to determine the error in radar reflectivity due to water vapor absorption. The retrieval algorithm has been developed using the vapor–liquid water ratio (VLWR) as well as both modeled and measured brightness temperatures for zenith to low elevation angles. Observation system simulation experiment (OSSE) results and measured radiosonde data have been used to determine that the retrieval uncertainty is less than 5% for integrated water vapor (IWV) and less than 12% for integrated liquid water (ILW). OSSE results for SWP show that the retrieval uncertainty is less than 8% at 5° elevation angle and less than 5% at 7° and 9°, while the mean difference between SWP retrieved from radiometer measurements and those retrieved from the S-PolKa radar during the DYNAMO campaign is less than 10% at 5° elevation angle and less than 7.5% at 7° and 9°. OSSE results for SLW show that the mean error is less than 24% for 5° elevation angle and less than 18% for 7° and 9°. Such retrievals of SWP and SLW help to characterize the distribution of water vapor and liquid water in the lower troposphere, which in turn may contribute to improvements in forecasting of convective initiation and precipitation.**

***Index Terms*—Atmospheric measurements, humidity, microwave radiometry, remote sensing, slant liquid water (SLW), slant water path.**

Manuscript received July 01, 2014; revised April 30, 2015; accepted May 29, 2015. This work was supported in part by the U.S. National Aeronautics and Space Administration, in part by the Science Mission Directorate, in part by the Earth Science Technology Office, as part of the Instrument Incubator Program under Grant NNX11AH05G and Grant NNX14AK70G.

S. Sahoo is with the School of Electrical and Electronics Engineering, Kalinga Institute of Industrial Technology University, Bhubaneswar 751024, India (e-mail: swaroop.sahoofel@kiit.ac.in).

X. Bosch-Lluis and S. C. Reising are with the Microwave Systems Laboratory, Department of Electrical and Computer Engineering, Colorado State University, Fort Collins, CO 80523 USA (e-mail: xavier.bosch-lluis@colostate.edu; steven.reising@colostate.edu).

S. M. Ellis and J. Vivekanandan are with the Earth Observing Laboratory, University Center for Atmospheric Research, Boulder, CO 80301 USA (e-mail: sellis@ucar.edu; vivek@ucar.edu).

P. Zuidema is with the Rosenstiel School of Marine and Atmospheric Science, University of Miami, Miami, FL 33149 USA (e-mail: pzuidema@rsmas.miami.edu).

Color versions of one or more of the figures in this paper are available online at http://ieeexplore.ieee.org.

Digital Object Identifier 10.1109/JSTARS.2015.2445785

I. Introduction

PRECIPITABLE water vapor (PWV) plays an important role in the initiation of both convection and precipitation [1], [2]. Continuous observations of PWV can be useful in forecasting both cloud formation and precipitation. Therefore, it is important to retrieve PWV with fine temporal and spatial resolution from remote sensing measurements. On the other hand, measuring cloud liquid water path (LWP) with high accuracy is required for understanding the impact of clouds on the Earth's climate and radiation budget [3]. Various algorithms and microwave instruments [4], [5] have been developed for retrieval of both integrated water vapor (IWV) and integrated liquid water (ILW) from measured brightness temperatures. Retrieval algorithms developed by Liljegren *et al.* [4] and used by Westwater [5] relate the mean radiating temperatures and measured microwave brightness temperatures at two frequencies to the total opacities at those frequencies. One of these frequencies is near the 22.235-GHz water vapor absorption line, and the other is between 29 and 33 GHz, in a window region that is primarily affected by liquid water. These total opacities are related to IWV and ILW through a linear relationship using statistically determined and site-specific retrieval coefficients [5], [6]. Some microwave radiometric retrieval algorithms also make use of *in-situ* surface meteorological measurements, including pressure, water vapor partial pressure, and temperature, to estimate IWV and ILW [4], [6]. A Bayesian optimal estimation retrieval technique has been used to retrieve the total liquid water content along with humidity and temperature profiles, in what is called the "integrated profiling technique" [7]. Total water vapor, liquid water, and ice content can be estimated from radiometer measurements using neural network-based inversions, as developed by Li *et al.* [8]. Hogg *et al.* [9] developed a steerable dual-frequency radiometer to retrieve slant water vapor path (SWP) and slant liquid water (SLW) at elevation angles of 20° and 90°, whereas Braun *et al.* [10] compared the SWP retrieved using a ground-based global positioning system (GPS) receiver with that using a

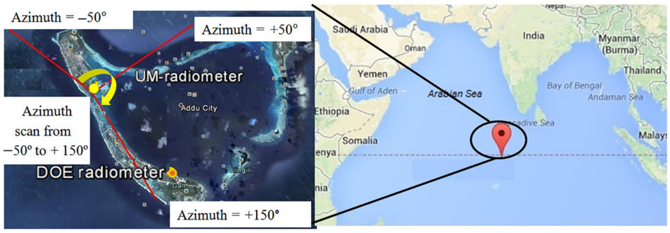

Fig. 1. (*Left*) Locations of the UM-radiometer (shown by the yellow disk in the upper left) and the DOE radiometer (shown by the orange disk in the lower middle) on Gan Island, Maldives. (*Right*) Location of the Maldive Islands in the equatorial Indian Ocean.

microwave radiometer to determine the accuracy of water vapor path retrieved at elevation angles above 10°. However, the retrieval of SWP and SLW from slant-path microwave radiometer measurements has not been explored in detail for elevation angles below 10°. Estimation of SWP and SLW at elevation angles below 10° can be useful to determine advection of water vapor and to improve understanding of cloud development in a particular area. This in turn can aid in precipitation forecasting, since the presence of clouds with high liquid water content is usually associated with precipitation and severe storms [9].

This work focuses on the development of a new retrieval strategy using the vapor–liquid water ratio (VLWR) to estimate SWP and SLW using ground-based brightness temperature measurements performed from zenith to low elevation angles during DYNAMO. This algorithm minimizes the squared differences between the measurements and the results from models developed using SWP and SLW from radiosondes launched from the nearby Department of Energy (DOE) Atmospheric Radiation Measurement (ARM) site. In this study, VLWR has been developed and its sensitivity to both water vapor and liquid water has been analyzed.

II. Experiment Description

The Dynamics of the Madden–Julian Oscillation (DYNAMO) [11] field campaign was conducted in the central equatorial Indian Ocean between September 1, 2011 and January 5, 2012 [12]. It was endorsed by the World Climate Research Programme and was led by research groups from the University of Miami and the University of Washington. The DYNAMO experiment was primarily designed to improve understanding of the Madden–Julian Oscillation (MJO) [13] and its initiation in that region based on observations of vertical moisture profiles, cloud structure, precipitation processes and planetary boundary layer properties. As part of the DYNAMO campaign, NCAR deployed the S-PolKa (dual-wavelength S- and Ka-bands) [14] radar, and the University of Miami deployed a two-channel microwave radiometer (UM-radiometer) [15]. The S-PolKa radar and the UM-radiometer were co-located on Gan Island in the Maldives in the equatorial Indian Ocean. A second two-channel microwave radiometer [15] was deployed at the U.S. DOE's ARM Site on Gan Island, approximately 8.5 km southeast of the UM-radiometer, as shown in Fig. 1. Both the UM-radiometer and the DOE radiometer have radiometer channels at the two measurement frequencies of 23.8 and 30.0 GHz. In addition, radiosondes were launched eight times daily (every 3 h) from the DOE ARM site during DYNAMO to provide *in-situ* data on atmospheric conditions. The S-PolKa radar was deployed to monitor clouds and to measure the intensity and type of precipitation. It performed 360° scans in azimuth and measured at elevation angles of 0.5°, 1.5°, 2.5°, 3.5°, 5.0°, 7.0°, 9.0°, and 11.0°.

The UM-radiometer performed brightness temperature measurements over a range of azimuth angles from −50° to +150° (referenced to north at 0°) and at elevation angles of 5°, 7°, 9°, 11°, 30°, 45°, and 90°. These brightness temperature measurements were performed continuously in time and have been used to estimate SWP and SLW during clear and cloudy skies.

III. Definition and Discussion of VLWR

Water vapor in the atmosphere strongly influences brightness temperatures at 23.8 GHz due to the proximity of this frequency to the water vapor absorption line at 22.235 GHz. On the other hand, 30.0 GHz is a window frequency between the water vapor line and the oxygen absorption complex near 60 GHz, so 30.0-GHz brightness temperatures are mostly affected by liquid water. Taking this into account, the VLWR is defined as the ratio of the brightness temperature at 23.8 GHz, $T_{B23.8}$, to that at 30.0 GHz, $T_{B30.0}$, as

$$\mathrm{VLWR}\,(\rho_v, \rho_l, P, T) = \frac{T_{B23.8}}{T_{B30.0}} \tag{1}$$

where ρ_v is the water vapor density, ρ_l is the liquid water density, P is the atmospheric pressure, and T is the physical temperature of the atmosphere.

Since VLWR is sensitive to changes in $T_{B23.8}$ and $T_{B30.0}$, it is sensitive to water vapor density, liquid water density, temperature, and pressure, as well as to scattering, which occurs principally in the presence of large water droplets and/or ice particles. Atmospheric temperature has a minimal effect on brightness temperatures at these frequencies. The pressure profile is typically slowly varying in time and has a second-order impact. Therefore, VLWR is principally sensitive to changes in water vapor ρ_v and liquid water ρ_l. This method is related to that used by Bosisio *et al.* [16] to analyze precipitation events.

A theoretical analysis has been performed to determine the sensitivity of VLWR to water vapor density ρ_v and liquid water density ρ_l. The sensitivities of VLWR to each of these quantities are considered separately to improve understanding of the fundamental relationships among these quantities. The derivation of the sensitivity of VLWR to water vapor and liquid water is based on the partial derivatives of the radiative transfer equation (RTE) at 23.8 and 30 GHz and is described in Appendix I of this paper.

A. VLWR Sensitivity to Water Vapor

Analyzing the sensitivity of VLWR to water vapor density using (I5), (I6), and (I7) in Appendix I involves calculation of $T_{B23.8}$ and $T_{B30.0}$ at a variety of elevation angles from 5° to 90°. This calculation is performed using 100 atmospheric profiles measured by radiosondes launched from the ARM site on

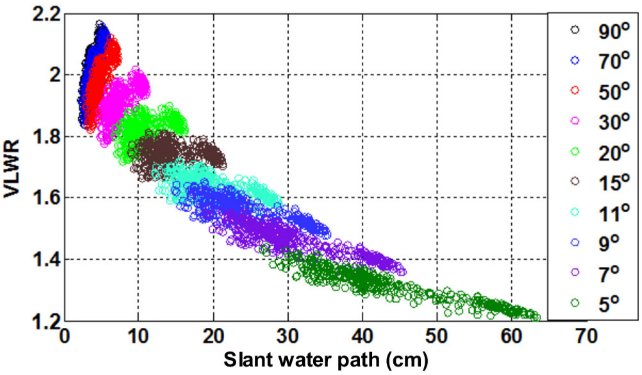

Fig. 2. VLWR values as a function of SWP for the range of SWP at elevation angles from 5° to 90°.

Gan Island during October 2011. In this analysis, the selected radiosondes were for clear sky conditions, so the liquid water density is set to zero in the simulations. The modeled VLWR values for elevation angles from 5° to 90° are based on simulated brightness temperatures and are shown in Fig. 2 as a function of SWP. VLWR is in the range of 1.8 to 2.2 for elevation angles from 50° to 90°, in the range of approximately 1.7 to 2 for elevation angles from 20° to 30°, and less than 1.7 for elevation angles from 5° to 11°. The VLWR values are approximately proportional to SWP for elevation angles from 30° to 90° and nearly independent of changes in SWP for elevation angles from 15° to 20°. In contrast, VLWR decreases as SWP increases for elevation angles from 5° to 11°.

Based on the simulation results and the theoretical water vapor sensitivity analysis, the sensitivity of VLWR to water vapor in the atmosphere, i.e., $\frac{\partial \mathrm{VLWR}}{\partial \rho_v}$, has three distinct regions, depending on the elevation angle of measurement, as explained below.

1) $\frac{\partial \mathrm{VLWR}}{\partial \rho_v} > 0$: The VLWR increases with water vapor density for elevation angles from 30° to 90°, as shown in Fig. 2. For this region, $\frac{\partial \alpha_{23.8v}(s)}{\partial \rho_v} \gg \alpha_{23.8v}(s) \frac{\partial \tau_{23.8v}}{\partial \rho_v}$ and $\frac{\partial \alpha_{30v}(s)}{\partial \rho_v} > \alpha_{30v}(s) \frac{\partial \tau_{30v}}{\partial \rho_v}$. An increase in the absorption coefficients at 23.8 and 30.0 GHz (due to an increase in water vapor density) has greater impact on VLWR sensitivity than an increase in path length due to increasing zenith angle does. However, 23.8 GHz is closer to the water vapor line; therefore, the sensitivity of the absorption coefficient at 23.8 GHz is greater than that at 30 GHz. Therefore, $\frac{\partial \alpha_{23.8v}(s)}{\partial \rho_v} - \alpha_{23.8v}(s) \frac{\partial \tau_{23.8v}}{\partial \rho_v} \gg \frac{\partial \alpha_{30v}(s)}{\partial \rho_v} - \alpha_{30v}(s) \frac{\partial \tau_{30v}}{\partial \rho_v}$, and consequently $A > B$.
2) $\frac{\partial \mathrm{VLWR}}{\partial \rho_v} \approx 0$: The VLWR is nearly independent of changes in water vapor density for elevation angles from 15° to 20°. For this region, $\frac{\partial \alpha_{23.8v}(s)}{\partial \rho_v} > \alpha_{23.8v}(s) \frac{\partial \tau_{23.8v}}{\partial \rho_v}$ and $\frac{\partial \alpha_{30v}(s)}{\partial \rho_v} > \alpha_{30v}(s) \frac{\partial \tau_{30v}}{\partial \rho_v}$. An increase in the sensitivity of the absorption coefficients at 23.8 and 30.0 GHz (due to an increase in water vapor density) is nearly balanced by an increase in path length due to increasing zenith angle. However, the sensitivity of the absorption coefficient at 23.8 GHz is still greater than that at 30 GHz. So, $\frac{\partial \alpha_{23.8v}(s)}{\partial \rho_v} - \alpha_{23.8v}(s) \frac{\partial \tau_{23.8v}}{\partial \rho_v} > \frac{\partial \alpha_{30v}(s)}{\partial \rho_v} - \alpha_{30v}(s) \frac{\partial \tau_{30v}}{\partial \rho_v}$ and $A \approx B$.
3) $\frac{\partial \mathrm{VLWR}}{\partial \rho_v} < 0$: The region in which VLWR decreases with increasing water vapor corresponds to elevation angles from 5° to 11°. For this region, $\frac{\partial \alpha_{23.8v}(s)}{\partial \rho_v} \approx \alpha_{23.8v}(s) \frac{\partial \tau_{23.8v}}{\partial \rho_v}$ and $\frac{\partial \alpha_{30v}(s)}{\partial \rho_v} > \alpha_{30v}(s) \frac{\partial \tau_{30v}}{\partial \rho_v}$, so $A < B$. An increase in path length due to increasing zenith angle has greater impact than an increase in the absorption coefficient at 23.8 GHz does (due to an increase in water vapor density). However, the sensitivity of the absorption coefficient at 30 GHz is still greater than that of path length. So, $\frac{\partial \alpha_{23.8v}(s)}{\partial \rho_v} - \alpha_{23.8v}(s) \frac{\partial \tau_{23.8v}}{\partial \rho_v} < \frac{\partial \alpha_{30v}(s)}{\partial \rho_v} - \alpha_{30v}(s) \frac{\partial \tau_{30v}}{\partial \rho_v}$, and consequently $A < B$.

This dependence of VLWR on elevation angle is due to both the distribution of water vapor in the atmosphere, which is larger near the ground, and the path length along the radiometer's field of view close to ground level since longer path lengths correspond to lower elevation angles.

B. *VLWR Sensitivity to Liquid Water*

The analysis in the previous section focuses on the sensitivity of VLWR to water vapor under clear sky conditions. Here, the effect of liquid water on VLWR is considered during nonprecipitating conditions. IWV is held constant at a value of 3.12 cm, where IWV is the same as SWP at 90° elevation angle, while the ILW (and by extension, SLW) is varied. Humidity profiles from radiosondes are used to compute liquid water density [6] profiles. The profiles of liquid water density and water vapor density are used to calculate absorption coefficients at 23.8 and 30.0 GHz using atmospheric absorption models [5] by Rosenkranz [17] and Liebe *et al.* [18] in this frequency range. Liquid water density is calculated from radiosonde data using [6] as

$$W = \begin{cases} 0 & \mathrm{RH} < b_0 \text{ or } T < 240\,K \\ 2\left(\frac{\mathrm{RH} - b_0}{30\%}\right)^2 & \mathrm{RH} > b_0 \text{ and } T > 240\,K \end{cases} \quad (2)$$

where

W liquid water density in $\mathrm{g/m^3}$;
RH relative humidity;
b_0 threshold relative humidity percentage for liquid water formation set at 85%;
T physical temperature.

Liquid water profiles are used to calculate the liquid water absorption coefficients as [19]

$$\alpha_{\mathrm{fliquid}} = 6\pi 10^{-2} \frac{\mathrm{Im}\{\epsilon_f\}}{|\epsilon_f + 2|^2} W f \quad (3)$$

where

$\alpha_{\mathrm{fliquid}}$ absorption coefficient in Np/km for the frequency f, i.e., 23.8 or 30.0 GHz;
f frequency;
ϵ_f relative dielectric constant of liquid water [18].

Liquid water absorption coefficients can vary based on the absorption model used, which in turn impacts the simulated brightness temperatures. Liquid water absorption coefficients are added to the dry and water vapor absorption coefficients, as in (I4). The total absorption $\alpha_f(s)$ is used in (I2a) and (I2b) to

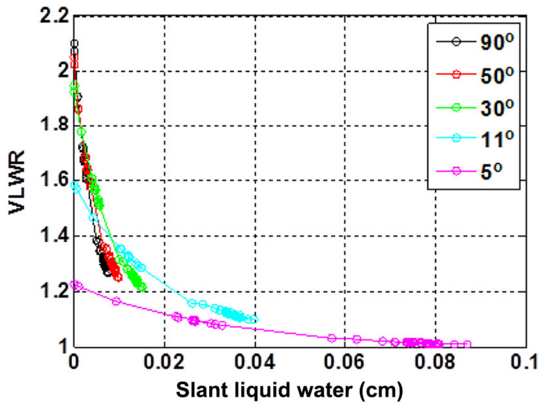

Fig. 3. VLWR values as a function of SLW for the range of SLW at elevation angles of 5°, 11°, 30°, 50°, and 90°.

simulate the values of $T_{B23.8}$ and $T_{B30.0}$, which are then used to calculate VLWR. Fig. 3 shows the relationship between VLWR and SLW at elevation angles of 5°, 11°, 30°, 50°, and 90°. Based on the above analysis, as the liquid water content increases, VLWR decreases to near unity as the brightness temperatures at 23.8 and 30.0 GHz become similar in value. However, the slope of the curves, or rate of decrease of VLWR with increase in SLW, increases (becomes more negative) as the elevation angle increases, as shown in Fig. 3.

Using the results in Fig. 3 and the theoretical sensitivity analysis of $\frac{\partial \mathrm{VLWR}}{\partial \rho_l}$, the sensitivity of VLWR to liquid water in the atmosphere has two distinct regions based on elevation angle.

1) $\frac{\partial \mathrm{VLWR}}{\partial \rho_l} \ll 0$: The first region with a large negative slope corresponds to elevation angles from 20° to 90°. For this region, $\frac{\partial \alpha_{30.0l}(s)}{\partial \rho_l} \gg \alpha_{30.0l}(s) \frac{\partial \tau_{30.0l}}{\partial \rho_l}$ (because the sensitivity of the absorption coefficient to the change in liquid water is much larger than the contribution due to optical depth at 30 GHz) and $\frac{\partial \alpha_{23.8l}(s)}{\partial \rho_l} > \alpha_{23.8l}(s) \frac{\partial \tau_{23.8l}}{\partial \rho_l}$. So, $\frac{\partial \alpha_{30.0l}(s)}{\partial \rho_l} - \alpha_{30.0l}(s) \frac{\partial \tau_{30.0l}}{\partial \rho_l} \gg \frac{\partial \alpha_{23.8l}(s)}{\partial \rho_l} - \alpha_{23.8l}(s) \frac{\partial \tau_{23.8l}}{\partial \rho_l}$ and $T_{B_{23.8}} > T_{B_{30.0}}$, and consequently $B \gg A$.

2) $\frac{\partial \mathrm{VLWR}}{\partial \rho_l} < 0$: The second region with a smaller negative slope corresponds to elevation angles of 11° or less. For this region, $\frac{\partial \alpha_{30.0l}(s)}{\partial \rho_l} > \alpha_{30.0l}(s) \frac{\partial \tau_{30.0l}}{\partial \rho_l}$ (because of the increased contribution due to optical depth at low elevation angles) and $\frac{\partial \alpha_{23.8l}(s)}{\partial \rho_l} > \alpha_{23.8l}(s) \frac{\partial \tau_{23.8l}}{\partial \rho_l}$. So, $\frac{\partial \alpha_{30.0l}(s)}{\partial \rho_l} - \alpha_{30.0l}(s) \frac{\partial \tau_{30.0l}}{\partial \rho_l} \geq \frac{\partial \alpha_{23.8l}(s)}{\partial \rho_l} - \alpha_{23.8l}(s) \frac{\partial \tau_{23.8l}}{\partial \rho_l}$ and $T_{B_{23.8}} > T_{B_{30.0}}$, and consequently $B \geq A$.

In addition, for liquid water, this dependence of VLWR on the elevation angle is due to the distribution of water vapor and liquid water in the atmosphere, as well as the path length of the atmosphere along the radiometer's field of view, with longer path lengths corresponding to lower elevation angles.

IV. Retrieval of IWV and ILW for Zenith Measurements

As seen in the previous section, VLWR is sensitive to liquid water and to some extent to water vapor, as well as the elevation angle of brightness temperature measurements. The sensitivity

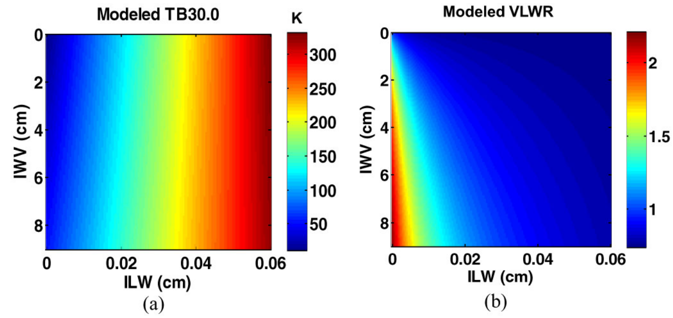

Fig. 4. (a) Modeled brightness temperatures in Kelvin at 30 GHz and (b) Modeled VLWR values for the range of IWV from 0 to 9 cm and the range of ILW from 0 to 0.06 cm.

of VLWR to these parameters allows retrieval of both IWV and ILW (both defined as total vertical column measurements) in the atmosphere and also the SWP and SLW as a function of elevation angle.

A. IWV and ILW Retrieval Algorithm

Based on results of the sensitivity analysis of VLWR, a retrieval algorithm was developed to estimate IWV and ILW, as shown in (4). This algorithm minimizes the sum of the squared differences between modeled and measured VLWRs and the squared differences between modeled and measured brightness temperatures at 30.0 GHz

$$\begin{aligned} \min_{\tau_{23.8},\ \tau_{30.0}} \chi^2 &= \left|\mathrm{VLWR}_{\mathrm{model}} - \mathrm{VLWR}'\right|^2 \\ &\quad + \left|T_{B30.0\,\mathrm{model}} - T'_{B30.0}\right|^2 \end{aligned} \tag{4}$$

where

$\mathrm{VLWR}_{\mathrm{model}}$	modeled VLWR for the range of IWV from 0 to 9 cm and the range of ILW from 0 to 0.06 cm;
VLWR'	VLWR calculated from measured brightness temperatures at 23.8 GHz and 30.0 GHz;
$T_{B30.0}$ and $T'_{B30.0}$	modeled and measured brightness temperatures at 30.0 GHz, respectively.

Brightness temperatures at 23.8 and 30.0 GHz are modeled using IWV and ILW from 700 radiosonde profiles collected at the ARM site on Gan Island during the months of June, July and August 2011. These data were interpolated to generate a brightness temperature model for the observed ranges of IWV (2.1 to 6.8 cm) and ILW (0 to 0.04 cm) for a zenith pointing radiometer, as shown in Fig. 4. However, the VLWR and $T_{B30.0}$ values modeled for the range of IWV from 0 to 2.1 cm and 6.8 to 9 cm as well as for the range of ILW from 0.04 to 0.06 cm have been extrapolated for this analysis, since the IWV values measured by radiosondes were in the range of 2.1 to 6.8 cm, and ILW values greater than 0.04 cm were not observed during the DYNAMO experiment.

The modeled VLWR was calculated using (1) and (I2a), and the results are shown in Fig. 4(b). The modeled VLWR is larger than 2.0 when the ILW is less than 0.005 cm and the IWV is greater than 2.8 cm. The modeled VLWR is less than or equal

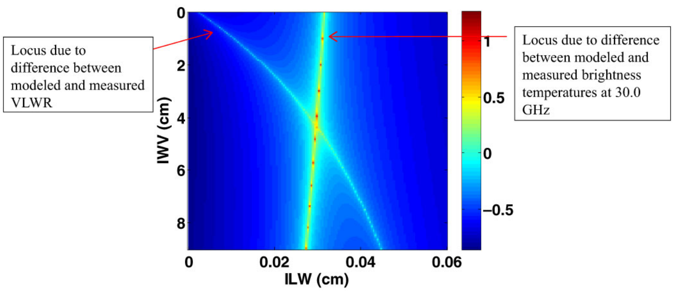

Fig. 5. Intersection of the two loci representing the two terms in (4) for brightness temperature measurements on December 15, 2011 at 05:30 UTC.

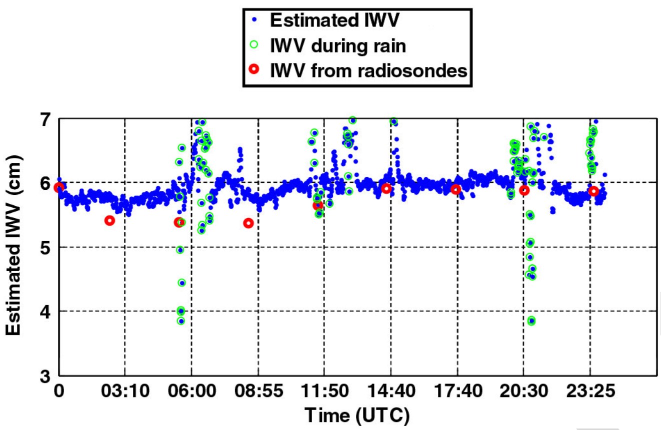

Fig. 6. Time series of estimated IWV from UM-radiometer measurements on December 15, 2011, in comparison with IWV from radiosonde measurements on the same day.

to unity for ILW values greater than 0.045 cm for all values of IWV considered. Modeled VLWR and $T_{B30.0}$ calculated in this way are used to retrieve IWV and ILW from brightness temperatures measured by the UM-radiometer on December 15, 2011 at 05:30 UTC. The results of this retrieval are shown in Fig. 5.

The curve starting near the y-axis and ending on the x-axis shows the locus of points, where the measured VLWR is equal to the modeled VLWR, i.e., the minimum of the first term in (4). From the first term, the VLWR (equal to 1.01 from measurements) could have been produced by a range of ILW from 0 to 0.045 cm and a range of IWV from 0 to 9 cm. The nearly vertical curve in the figure shows the locus of points where the measured $T'_{B30.0}$ and modeled $T_{B30.0}$ are equal, i.e., the minimum of the second term in (4). From the second term, the measured $T'_{B30.0}$ could have been produced by a range of IWV from 0 to 9 cm but by only a narrow range of ILW, from 0.025 to 0.035 cm. From the intersection of the two loci in Fig. 5, the estimated values of the IWV and ILW are found to be 4.36 cm and 0.032 cm, respectively.

This algorithm has been used to retrieve time series of IWV and ILW for December 15, 2011, as shown in blue in Figs. 6 and 7, respectively. IWV and ILW retrieved during precipitating conditions are represented by the green circles around the corresponding blue points. Precipitating conditions are defined as when the VLWR value is below an empirically determined threshold value of 1.2, based on the mean VLWR determined

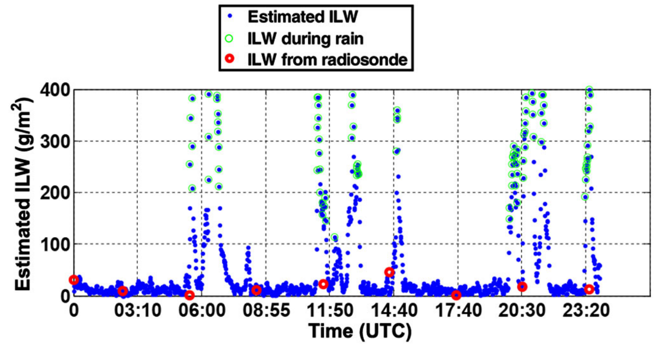

Fig. 7. Time series of estimated ILW from UM-radiometer measurements on December 15, 2011, in comparison with ILW from radiosonde measurements on the same day.

for a variety of light precipitation events measured during DYNAMO. The red circles in Figs. 6 and 7 show the IWV and ILW, respectively, calculated from measurements using the nine radiosondes launched on December 15, 2011.

Retrieved IWV and ILW compare well with the IWV and ILW measured by radiosondes. However, the IWV and ILW from radiosondes launched at 02:30, 05:30 and 08:30 UTC exhibit lower values of IWV than the retrieved values. This is believed to be due to the fact that the DOE ARM radiosonde launch site was 8.5 km southeast of the UM-radiometer, and there was significant variability of water vapor and liquid water on this spatial scale during that time period.

B. Observation System Simulation Experiment and Retrieval Performance of a Zenith-Pointing Radiometer

An observation system simulation experiment (OSSE) was performed to determine the uncertainty associated with the retrieval algorithm used in the previous section. As part of the OSSE, atmospheric measurements from 500 radiosondes launched from the ARM site on Gan Island during August and September 2011 were used to simulate brightness temperatures at 23.8 and 30.0 GHz, from which the IWV and ILW were estimated using (4). The uncertainty associated with the IWV retrieval algorithm was calculated as the difference between the estimated IWV and that measured by radiosondes. The average IWV retrieval uncertainty was calculated in each of 10 bins of 0.25 cm width, and is shown in Fig. 8 to be 3.5%–4.5% for IWV values from 4.0 to 6.5 cm.

Similarly, the uncertainty associated with the ILW retrieval algorithm was calculated as the difference between the estimated ILW and that measured by radiosondes. The average ILW retrieval uncertainty was calculated in each of 7 bins of 0.004 cm width, shown in Fig. 9 as 12% for ILW of 0.005 cm, decreasing to 4% for ILW of 0.0175 cm or greater and decreasing to 3% for ILW of 0.0275 cm or greater. Retrieval uncertainties in both IWV and ILW from the OSSE have generally similar values to the difference between retrieved values from UM-radiometer data and interpolated values from radiosondes during DYNAMO, as shown in Figs. 8 and 9, respectively. The retrieval uncertainties from DYNAMO presented in Figs. 8 and 9 have been calculated for zenith measurements performed during the period of December 1–15, 2011.

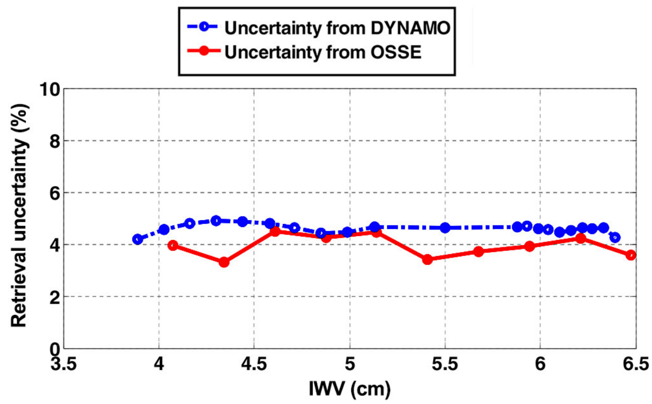

Fig. 8. IWV retrieval uncertainty from OSSE (in red) and difference between radiometer retrievals and radiosonde data measured during DYNAMO (in blue).

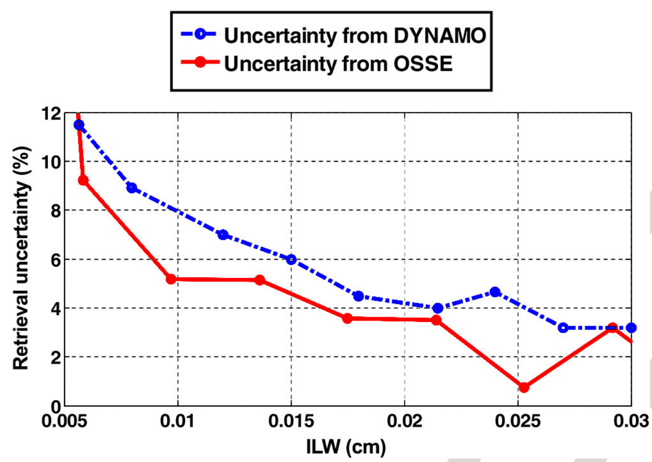

Fig. 9. ILW retrieval uncertainty from OSSE (in red) and difference between radiometer retrievals and radiosonde data measured during DYNAMO (in blue).

V. Retrieval of SWP and SLW for Low Elevation Angle Measurements

Microwave radiometer measurements performed at a variety of azimuth angles from zenith to low elevation angles are used to retrieve SWP and SLW using (4). Models for $T_{B23.8}$ and $T_{B30.0}$ at 5°, 7°, 9°, and 11° elevation angles were developed for a range of SWP and SLW. SWP and SLW have been retrieved for October 11, 2011, at 21:35 UTC at the four low elevation angles and at azimuth angles from -50° to $+150^\circ$. The retrieved SWP and SLW are shown in Fig. 10(a) and (b), respectively, on a director cosine plane, where θ and ϕ are the zenith and azimuth angles of measurement, respectively. For elevation angles of 5° and 7°, retrieved SWP is from 27 cm to 65 cm, and it is from 20 cm to 42 cm for elevation angles of 9° and 11°. Similarly, retrieved SLW for elevation angles of 5° and 7° is from 0.05 to 0.37 cm, and it is from 0.05 to 0.17 cm for elevation angles of 9° and 11°.

The SLW at the elevation angle of 5° and azimuth angles of -42°, 60° to 90°, and 95° to 105° are greater than at the other azimuth angles. These correspond to precipitation, since the VLWR values are between 1 and 1.1, i.e., below the empirical precipitation threshold of 1.2. The radar reflectivity

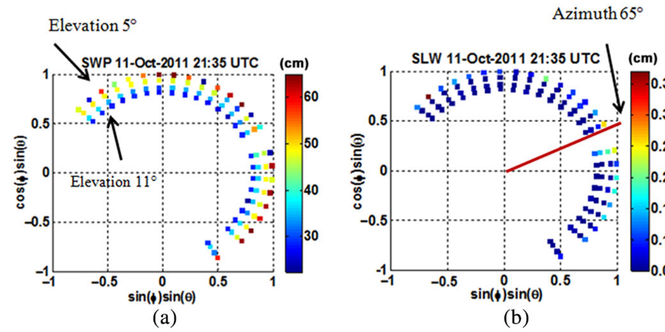

Fig. 10. (a) Retrieved SWP and (b) SLW on October 11, 2011, at 21:35 UTC for all azimuth angles measured and elevation angles of 5°, 7°, 9°, and 11°.

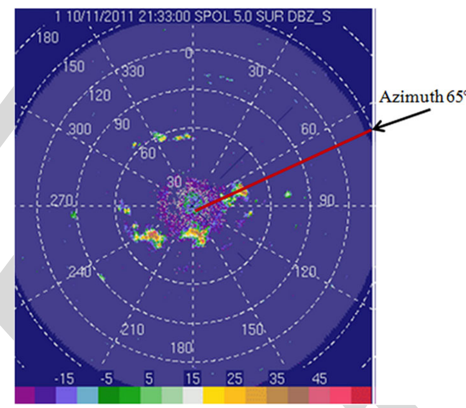

Fig. 11. Radar reflectivity PPI image at 5° elevation angle on October 11, 2011 at 21:33 UTC [20].

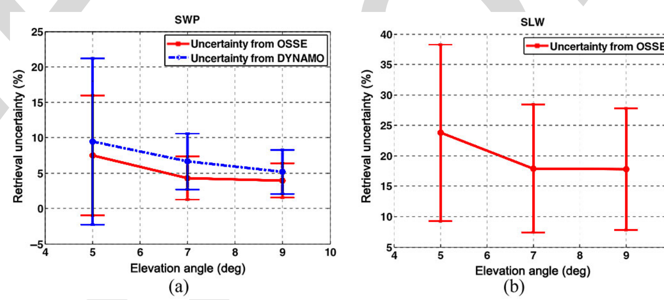

Fig. 12. (a) Retrieval uncertainty of SWP at elevation angles of 5°, 7°, and 9° based on an OSSE (in red). Comparison between radar- and radiometer-retrieved values of SWP (in blue). (b) Retrieval uncertainty of SLW at elevation angles of 5°, 7°, and 9° based on an OSSE (in red).

plan position indicator (PPI) image in Fig. 11 [20] shows measured precipitation with a reflectivity of 20–35 dBZ along the red segment at 65° azimuth angle.

The performance of the retrieval algorithm for SWP and SLW at low elevation angles is assessed using an OSSE along with comparison of SWP radiometer retrievals with SWP radar retrievals during the DYNAMO campaign. To implement the OSSE, radiosonde-measured profiles are used to simulate $T_{B23.8}$ and $T_{B30.0}$, which are then used to estimate SWP and SLW at elevation angles of 5°, 7° and 9°. Uncertainties associated with the retrieval algorithm were calculated as the difference between the estimated SWP and SLW and the corresponding quantities measured by radiosondes, with results as shown in Fig. 12.

Next, SWP were retrieved using two independent measurement sources, the UM-radiometer and the NCAR S-PolKa radar, colocated during the DYNAMO experiment. To compare SWP retrievals, the radar and radiometer performed simultaneous measurements at 5°, 7° and 9° elevation angles to sample common volumes of the atmosphere. The SWP retrievals from the radar and radiometer are based on different principles due to different measurement physics. The radar measures the attenuation of the signal due to water vapor from the radar to the edge of a cloud or precipitation echo, so the range may vary substantially from measurement to measurement [21], [22]. The retrieval of SWP from radar involves comparison of the reflectivity from the edges of clouds and precipitation at 2.8 GHz (S-band), which is not significantly attenuated by water vapor, with those at 35 GHz (Ka-band), which is significantly attenuated. The attenuation value is then used to estimate the SWP. In contrast, radiometers provide a more consistent range for SWP retrieval, although large values of attenuation often limit the range of the radiometer, depending on the atmospheric conditions. For comparison of the two retrievals, the radiometer-retrieved SWP is normalized by the equivalent range of the atmosphere measured by the radiometer and scaled by the radar range over which attenuation is measured. The equivalent radiometer range for a particular elevation angle has been computed using the path length of the atmosphere in the direction of the radiometer field of view from which 95% of the total measured power is emitted, as described in Appendix B. Based on a planar atmosphere model, the equivalent radiometer ranges have been calculated as 50, 44, and 37 km for elevation angles of 5°, 7°, and 9°, respectively.

Finally, the radar-retrieved SWP values are subtracted from the range-adjusted radiometer-retrieved SWP values to calculate the mean difference at each elevation angle as a percentage, as shown in the blue points in Fig. 12(a), with error bars showing the standard deviation of the differences. The differences between these SWP retrievals are less than 10% for 5° elevation angle, decreasing to less than 7.5% for 7° and 9° elevation angles. Differences may be due to uncertainties in the retrieval from both the radar and radiometer, as well as to uncertainties in the range normalization for the radiometer-retrieved values. Furthermore, it can be observed that both the mean difference and its standard deviation decrease as the elevation angle increases. This is due to uncertainties that decrease at higher elevation angles since the equivalent radiometer range is typically longer than the actual radar range. For comparison, the percentage mean error in SWP from the OSSE is less than 8% at 5° elevation angle and less than 5% at 7° and 9° elevation angles. The OSSE percentage errors are consistently approximately 2% lower than the differences between SWP retrieved from radar and that retrieved from radiometer measurements during DYNAMO.

The performance of the retrieval technique for estimation of SLW is based on OSSE results only because no SLW information is available from the radar measurements. Fig. 12(b) shows the error of the retrieved SLW at 5°, 7°, and 9°elevation angles. Exhibiting similar behavior to SWP in elevation angle with different magnitudes, the error is less than 24% at 5° elevation angle and decreasing with increasing elevation angle to less than 18% at 7° and 9° elevation angles.

VI. Summary and Conclusion

In this paper, a new retrieval strategy has been developed to retrieve SWP and SLW from ground-based microwave radiometer measurements from zenith to low elevation angles. To accomplish this, the VLWR has been defined as the ratio of the brightness temperature at 23.8 GHz to that at 30.0 GHz. The sensitivities of VLWR to both atmospheric water vapor and liquid water are found to change substantially with the elevation angle of radiometer measurements. Fig. 2 shows the behavior of VLWR due to changes in SWP and elevation angles during clear sky conditions. Fig. 3 shows the trend of VLWR for changes in SLW at various elevation angles during nonprecipitating conditions. SLW and SWP have been kept constant for Figs. 2 and 3, respectively. The algorithm for retrieval of water vapor and liquid water in the atmosphere is based on minimization of the sum of the squared difference between modeled and measured VLWR and the squared difference between modeled and measured 30.0-GHz brightness temperatures. The modeled values of VLWR and $T_{B30.0}$ for a range of IWV and ILW are shown in Fig. 4. Interpolation has been performed to determine the models for the range of IWV from 2.1 to 6.8 cm and the range of ILW from 0 to 0.04 cm. However, extrapolation has been used instead of interpolation to determine the models for the ranges of IWV from 0 to 2.1 cm and from 6.8 to 9 cm as well as the range of ILW from 0.04 to 0.06 cm. The extrapolated values for the range of IWV from 6.8 to 9 cm and the range of ILW from 0.04 to 0.06 cm are higher than the highest realistic atmospheric values, but they do not affect the retrieval for nonprecipitating conditions. Scattering has not been considered while modeling the VLWR and $T_{B30.0}$, so the retrieval will have larger errors than usual when the models are applied to medium to heavy precipitating conditions.

The new retrieval strategy was validated using ground-based University of Miami (UM) microwave radiometer (UM-radiometer) measurements at 23.8 and 30.0 GHz performed on Gan Island during the DYNAMO Experiment. Retrievals of IWV and ILW from zenith pointing UM-radiometer measurements show good agreement between these quantities and those calculated from radiosonde measurements, with differences of less than 5% and 12% for IWV and ILW, respectively, where IWV is for all weather conditions, and ILW includes cloudy and precipitating conditions. The differences for ILW retrievals are 12% for the lowest ILW values and rapidly decrease with increasing ILW to less than 4% for ILW values greater than 0.0175 cm. The differences between IWV and ILW retrieved from UM-radiometer measurements and those calculated from radiosonde measurements agree well with retrieval uncertainties found using an OSSE.

The new retrieval strategy was also used to estimate SWP and SLW from UM-radiometer measurements at low elevation angles during DYNAMO. To the authors' knowledge, this is the first time that microwave radiometer-retrieved SWP has been validated by comparison with radar-retrieved SWP, showing a mean difference of less than 10% at 5° elevation angle and less than 7.5% at 7° and 9° elevation angles, decreasing as the elevation angle increases. These mean differences and their dependence on elevation angle agree well with SWP retrieval uncertainties found using an OSSE. For liquid water, the OSSE shows that the retrieval error in SLW is less than 24% at 5° elevation angle, decreasing to less than 18% at 7° and 9° elevation angles. Such retrievals of SWP and SLW are useful for characterizing the spatial and temporal variation in the distribution of water vapor and liquid water in the lower troposphere, which may in turn contribute to improvements in forecasting of convective initiation and precipitation.

Appendix I

The partial derivative of VLWR with respect to either water vapor density or liquid water density is given by

$$\frac{\partial VLWR}{\partial \rho_x} = \frac{\partial \left(\frac{T_{B_{23.8}}}{T_{B_{30.0}}}\right)}{\partial \rho_x} = \frac{T_{B_{30.0}}\left(\frac{\partial T_{B_{23.8}}}{\partial \rho_x}\right) - \left(\frac{\partial T_{B_{30}}}{\partial \rho_x}\right) T_{B_{23.8}}}{\left(T_{B_{30.0}}\right)^2} \tag{I1}$$

where ρ_x is the density variable, and x represents v for water vapor density or l for liquid water density.

Brightness temperatures at 23.8 and 30.0 GHz may be simulated using the RTE [5] given by

$$T_{B_f} = \int_0^\infty T(s)\,\alpha_f(s)\,e^{-\tau_f(0,s)}\sec(\theta)\,ds + T_{b0}e^{-\tau_f(0,\infty)} \tag{I2a}$$

$$\tau_f(0,s) = \int_0^s \alpha_f(s')\sec(\theta)\,ds' \tag{I2b}$$

where

- $T(s)$ physical temperature of the atmosphere at height s above the ground;
- $\alpha_f(s)$ absorption coefficient at height s above the ground at frequency f, and $\alpha_f(s) = \alpha_{fdry}(s) + \alpha_{fvapor}(s) + \alpha_{fliquid}(s)$, in which α_{fdry} is the dry component of the absorption coefficient, and α_{fvapor} and $\alpha_{fliquid}$ are the components of the absorption coefficient due to water vapor and liquid water, respectively [17], [18];
- τ_f atmospheric opacity at frequency f;
- T_{b0} cosmic background brightness temperature (2.73 K, constant at these frequencies);
- θ zenith angle.

The RTE in (I2) takes into consideration that the diameter of water droplets in clouds is very small compared to the wavelength of the radiation, so the Rayleigh approximation can be used. Based on this approximation, only absorption models are used, and scattering can be neglected in the RTE. Continuing the derivation, the partial derivative of T_{B_f} with respect to ρ_x is

$$\begin{aligned}\frac{\partial T_{B_f}}{\partial \rho_x} &\cong \frac{\partial}{\partial \rho_x}\int_0^\infty T(s)\,\alpha_f(s)\,e^{-\tau_f(0,s)}\sec(\theta)\,ds \\ &= \int_0^\infty T(s)\,\frac{\partial}{\partial \rho_x}\left[\alpha_f(s)\,e^{-\tau_f(0,s)}\right]\sec(\theta)\,ds \\ &= \int_0^\infty T(s)\,e^{-\tau_f(0,s)}\left[\frac{\partial \alpha_f(s)}{\partial \rho_x} - \alpha_f(s)\frac{\partial \tau_f}{\partial \rho_x}\right]\sec(\theta)\,ds\end{aligned} \tag{I3}$$

where the cosmic background temperature T_{b0} has been omitted due to its minimal impact on the calculated brightness temperature. $\frac{\partial \alpha_f(s)}{\partial \rho_x}$ in (I3) consists of a dry component as well as components due to water vapor and liquid water, as

$$\frac{\partial \alpha_f(s)}{\partial \rho_x} = \frac{\partial \alpha_{fdry}(s)}{\partial \rho_x} + \frac{\partial \alpha_{fvapor}(s)}{\partial \rho_x} + \frac{\partial \alpha_{fliquid}(s)}{\partial \rho_x}. \tag{I4}$$

The partial derivatives of the absorption coefficients at frequency f in (I4) are principally dependent on density ($\rho_x(s)$) and to a lesser extent on temperature and atmospheric pressure [17]. In addition, those parameters that vary most rapidly in time are the water vapor density and liquid water density, while the atmospheric temperature and pressure vary more slowly. The value of $\frac{\partial \alpha_f(s)}{\partial \rho_x} - \alpha_f(s)\frac{\partial \tau_f}{\partial \rho_x}$ changes with the value of ρ_x and also with the zenith angle of the measurement, θ, as shown in (I2b). The factor $\frac{\partial \alpha_f(s)}{\partial \rho_x} - \alpha_f(s)\frac{\partial \tau_f}{\partial \rho_x}$ is positive when $\frac{\partial \alpha_f(s)}{\partial \rho_x} > \alpha_f(s)\frac{\partial \tau_f}{\partial \rho_x}$, which occurs at low zenith angles, i.e., at high elevation angles. In that case, the measured brightness temperature increases linearly with ρ_x, as shown in Fig. 2 and explained in Section III-A. On the other hand, as the zenith angle θ increases, i.e., the elevation angle decreases, the value of the term $\frac{\partial \alpha_f(s)}{\partial \rho_x}$ approaches that of $\alpha_f(s)\frac{\partial \tau_f}{\partial \rho_x}$, resulting in $\frac{\partial \alpha_f(s)}{\partial \rho_x} \approx \alpha_f(s)\frac{\partial \tau_f}{\partial \rho_x}$. Substituting (I2) and (I3) into (I1), we obtain

$$\frac{\partial}{\partial \rho_x}(VLWR) = \frac{A-B}{\left(T_{B_{30.0}}\right)^2} \tag{I5}$$

where

$$\begin{aligned}A = T_{B_{30.0}}\int_0^\infty T(s)\,e^{-\tau_{23.8}(0,s)}\Bigg[&\frac{\partial \alpha_{23.8}(s)}{\partial \rho_x} \\ &-\alpha_{23.8}(s)\frac{\partial \tau_{23.8}}{\partial \rho_x}\Bigg]\sec(\theta)\,ds\end{aligned} \tag{I6}$$

$$\begin{aligned}B = T_{B_{23.8}}\int_0^\infty T(s)\,e^{-\tau_{30.0}(0,s)}\Bigg[&\frac{\partial \alpha_{30.0}(s)}{\partial \rho_x} \\ &-\alpha_{30.0}(s)\frac{\partial \tau_{30.0}}{\partial \rho_x}\Bigg]\sec(\theta)\,ds.\end{aligned} \tag{I7}$$

The term $\left(T_{B_{30.0}}\right)^2$ exhibits a monotonically increasing positive dependence on both water vapor density ρ_v and liquid water density ρ_l. It changes the magnitude of the derivative in (I5), but the sign of the derivative is determined by the relative values of A and B. The two terms A and B are dependent on both water vapor density and liquid water density. Their values determine whether the overall VLWR in (I5) has either a positive, negative or relatively little dependence on ρ_x.

Appendix II

A simulation-based study is performed to determine the equivalent range of a microwave radiometer at a variety of elevation angles. The atmosphere is considered to be horizontally stratified as in Fig. 13, and most of the water vapor is assumed to be in the lowest 10 km of the troposphere.

First, brightness temperatures are simulated for each frequency using the RTE given by (I2) up to 10 km altitude in

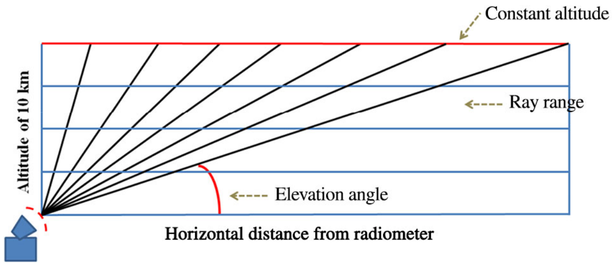

Fig. 13. Radiometer scanning at a variety of elevation angles.

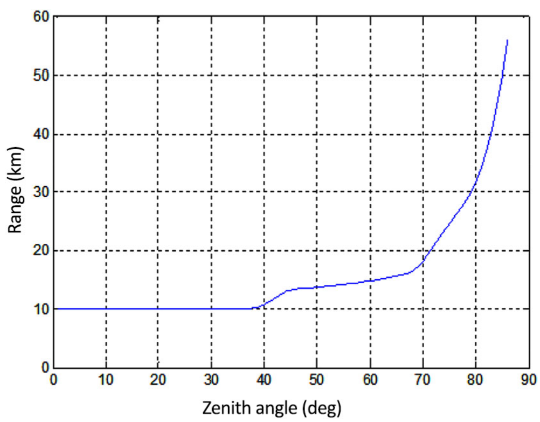

Fig. 14. Dependence of the radiometric range on zenith angle.

the troposphere, without considering the radiometer range, as shown in Fig. 13. Then, brightness temperatures are again simulated using the RTE corresponding to each elevation angle, this time constraining the range instead of the altitude. The range for which the brightness temperature calculated in the second step is 95% of that simulated in the first step is considered the actual radiometer range. This process is repeated for elevation angles of 90° to 5° to find the radiometer range with respect to elevation angle. The radiometer range depends upon the amount of atmospheric attenuation, which in turn varies with changes in the temperature and water vapor density in the atmosphere. To take into account this uncertainty, the radiometer range is calculated for a variety of atmospheric conditions over a wide range of temperature and water vapor density, including cases of light precipitation.

As shown in Fig. 14, the equivalent radiometer range is 10 km for zenith angles of 0° to 35°, and it increases from 10 to 55 km for zenith angles of 35° to 85°. The standard deviation of range is 1 km for 0° zenith angle and increases to 5 km for 85° zenith angle. These equivalent ranges have been calculated for weather conditions at Gan Island during the DYNAMO experiment, and they are expected to change for different locations and weather conditions.

REFERENCES

[1] L. J. Battan and A. R. Kassander, "Design of a program of randomized seeding of orographic cumuli," *J. Meteor.*, vol. 17, pp. 583–590, 1960.

[2] K. E. Trenberth, J. Fasullo, and L. Smith, "Trends and variability in column-integrated atmospheric water vapor," *Clim. Dyn.*, vol. 24, pp. 741–758, May 2005.

[3] B. A. Wielicki, R. D. Cess, M. D. King, D. A. Randall, and E. F. Harrison, "Mission to Planet Earth: Role of clouds and radiation in climate," *Bull. Amer. Meteor. Soc.*, vol. 76, pp. 2125–2153, 1995.

[4] J. C. Liljegren, E. E. Clothiaux, G. G. Mace, S. Kato, and X. Dong, "A new retrieval for cloud liquid water path using a ground-based microwave radiometer and measurements of cloud temperature," *J. Geophys. Res.*, vol. 106, no. D13, pp. 14485–14500, Jul. 2001.

[5] E. R. Westwater, "Ground-based microwave remote sensing of meteorological variables," in *Atmospheric Remote Sensing by Microwave Radiometry*, M. A. Janssen, Ed. New York, NY, USA: Wiley, 1993, pp. 145–214.

[6] C. Mätzler and J. Morland, "Refined physical retrieval of integrated water vapor and cloud liquid for microwave radiometer data," *IEEE Trans. Geosci. Remote Sens.*, vol. 47, no. 6, pp. 1585–1594, Jun. 2009.

[7] U. Löhnert, S. Crewell, and C. Simmer, "An integrated approach toward retrieving physically consistent profiles of temperature, humidity, and cloud liquid water," *J. Appl. Meteor.*, vol. 43, pp. 1295–1307, Sep. 2004.

[8] L. Li, J. Vivekanandan, C. H. Chan, and L. Tsang, "Microwave radiometric technique to retrieve vapor, liquid and ice, Part I—Development of neural network-based inversion method," *IEEE Trans. Geosci. Remote Sens.*, vol. 35, no. 2, pp. 224–236, Mar. 1997.

[9] D. C. Hogg, F. O. Guiraud, J. B. Snider, M. T. Decker, and E. R. Westwater, "A steerable dual-channel microwave radiometer for measurement of water vapor and liquid in the troposphere," *J. Clim. Appl. Meteor.*, vol. 22, pp. 789–806, May 1983.

[10] J. Braun, C. Rocken, and J. Liljegren, "Comparisons of line-of-sight water vapor observations using the Global Positioning System and a pointing microwave radiometer," *J. Atmos. Ocean. Technol.*, vol. 20, pp. 606–612, 2003.

[11] University Corporation for Atmospheric Research. (2010, Jan.). *DYNAMO Documentation* [Online]. Available: http://www.eol.ucar.edu/projects/dynamo/documents/index.html, accessed on: May 28, 2014.

[12] University Corporation for Atmospheric Research. (2011). *DYNAMO Data Access* [Online]. Available: http://data.eol.ucar.edu/master_list/?project=DYNAMO, accessed on: May 28, 2014.

[13] C. Zhang, "Madden–Julian oscillation," *Rev. Geophys*, vol. 43, no. 2, pp. 1–36, Jun. 2005.

[14] G. Farquharson *et al.*, "NCAR S-Pol second frequency (Ka-band) radar," in *Proc. 32nd Conf. Radar Meteorol.*, Albuquerque, NM, USA, 2005, pp. 1–4.

[15] M. P. Cadeddu. (2012, May 01). *Microwave Radiometer—3 Channel (MWR3C) Handbook* [Online]. Available: http://www.arm.gov/publications/tech_reports/handbooks/mwr3c_handbook.pdf?id=24, accessed on: May 28, 2014.

[16] A. V. Bosisio, P. Ciotti, E. Fionda, and A. Martellucci, "A sky status indicator to detect rain-affected atmospheric thermal emissions observed at ground," *IEEE Trans. Geosci. Remote Sens.*, vol. 51, no. 9, pp. 4643–4649, Sep. 2013.

[17] P. W. Rosenkranz, "Water vapor microwave continuum absorption: A comparison of measurements and models," *Radio Sci.*, vol. 33, no. 4, pp. 919–928, Jul./Aug. 1998.

[18] H. J. Liebe, G. A. Hufford, and T. Manabe, "A model for the complex permittivity of water at frequencies below 1 THz," *Int. J. Infrared Millimeter Waves*, vol. 12, no. 7, pp. 659–675, 1991.

[19] A. J. Gasiewski, "Microwave radiative transfer in hydrometeors," in *Atmospheric Remote Sensing by Microwave Radiometry*, M. A. Janssen, Ed. Hoboken, NJ, USA: Wiley, 1993, pp. 91–144.

[20] B. Rilling. (2012). *Radar Image Archive*. NCAR, Boulder, CO, USA [Online]. Available: http://www.eol.ucar.edu/rsf/image_archive/dynamo/spol/sur/, accessed on: Dec. 12, 2014.

[21] S. M. Ellis and J. Vivekanandan, "Water vapor estimates using simultaneous dual-wavelength radar observations," *Radio Sci.*, vol. 45, no. 5, pp. 1–15, Oct. 2010, doi: 10.1029/2009RS004280.

[22] R. Meneghini, L. Liao, and L. Tian, "A feasibility study for simultaneous estimates of water vapor and precipitation parameters using a three-frequency radar," *J. Appl. Meteor.*, vol. 44, pp. 1511–1525, Oct. 2005.

Swaroop Sahoo received the B.Tech. degree in electrical engineering from the Biju Pattnaik University of Technology, Bhubaneswar, India, in 2005, and the M.S. and Ph.D. degrees in electrical engineering from Colorado State University, Fort Collins, CO, USA, in May 2011 and May 2015, respectively.

He developed a new algorithm to retrieve slant water path and slant liquid water using radiometer measurements at low elevation angles.

Xavier Bosch-Lluis received the Master's degree in telecommunication engineering specialized in communications systems, the Master of Science degree in research on information and communication technologies (MERIT), the Master's degree in electronics engineering, and the Ph.D. degree in department of signal theory and communications from the Universitat Politècnica de Catalunya (UPC) in 2005, 2007, 2010, and 2011, respectively.

Since April 2011, he has been a Post-Doctoral Researcher with the Microwave Systems Laboratory, Electrical and Computer Engineering Department, Colorado State University, Fort Collins, CO, USA. His research interests include developing innovative radiometer systems and retrieval algorithms for passive microwave and millimeter-wave remote sensing.

Steven C. Reising (S'88–M'98–SM'04) received the B.S.E.E. (*magna cum laude*) and M.S.E.E. degrees in electrical engineering from Washington University in St. Louis, Saint Louis, MO, USA, and the Ph.D. degree in electrical engineering from Stanford University, Stanford, CA, USA, in 1998.

He has been a Full Professor of Electrical and Computer Engineering with Colorado State University (CSU), Fort Collins, CO, USA, since July 2011, where he served as Associate Professor from August 2004 to June 2011. Before joining the CSU faculty in 2004, he served as an Assistant Professor of Electrical and Computer Engineering with the University of Massachusetts Amherst, Amherst, MA, USA, where he received tenure. He served as a Summer Faculty Fellow for three summers in the Remote Sensing Division, Naval Research Laboratory, Washington, DC, USA. He has been the Principal Investigator of more than 12 grants from the National Science Foundation (NSF), NASA, Office of Naval Research (ONR), National Polar-orbiting Operational Environmental Satellite System Integrated Program Office, European Space Agency, and Ball Aerospace and Technologies Corporation. His research interests include a broad range of remote sensing disciplines, including passive microwave and millimeter-wave remote sensing of the oceans, atmosphere, and land; microwave and millimeter-wave integrated circuits and radiometer systems; lidar systems for sensing of temperature and winds in the middle and upper atmosphere; atmospheric electrodynamics; and low-frequency remote sensing of lightning and its energetic coupling to the ionosphere, which produces chemical changes and optical emissions.

Dr. Reising serves as the Vice President of Information Resources (2011–present) and formerly as the Vice President of Technical Activities (2008–2010) of the IEEE Geoscience and Remote Sensing Society (GRSS). He has been serving as an elected member of the IEEE Microwave Theory and Techniques Society (MTT-S) Administrative Committee (AdCom) since January 2014, for which he is currently a Chair of the Inter-Society Committee. He has been serving as an elected member of the IEEE GRSS AdCom continuously since 2003, after 3-year terms as Editor of the GRSS Newsletter (2000–2002) and Associate Editor for University Profiles (1998–2000). He was an Associate Editor of the IEEE Transactions on Geoscience and Remote Sensing Letters (GRSL) from its founding in 2004 to 2013. He has been a Guest Editor of IEEE Transactions on Geoscience and Remote Sensing (TGRS) for the International Geoscience and Remote Sensing Symposium (IGARSS) 2012 Special Issue published in September 2013, the IGARSS 2008 Special Issue published in November 2009, and the Special Issue on Microwave Radiometry and Remote Sensing Applications published in July 2007. He has served as a Reviewer for TGRS, GRSL, the IEEE Transactions on Microwave Theory and Techniques, *Remote Sensing of Environment, the Journal of Atmospheric and Oceanic Technology, the Journal of Geophysical Research—Oceans, Geophysical Research Letters, Marine Geodesy, Atmospheric Chemistry and Physics, the Journal of Oceanography*, and *Radio Science*. In organizing scientific meetings, he was one of two Technical Program Co-Chairs of the IEEE IGARSS 2008 in Boston, MA, USA, with over 1700 attendees. He served as the General Chair of MicroRad'06, the 9th Specialist Meeting on Microwave Radiometry, held in March 2006 in San Juan, Puerto Rico, with 126 attendees from 15 countries. He was the Local Arrangements Chair for IGARSS 2006 in Denver, with over 1250 attendees. He has been an active participant in each IGARSS Technical Program Committee from 2001–present. He serves the URSI as the Immediate Past Chair (2015–2017), and previously as Chair (2012–2014), and Secretary and Chair-Elect (2009–2011) of its USNC, consisting of ten scientific commissions focusing on the theory and applications of electromagnetics and radio waves from ultra-low frequencies to Terahertz. He chaired the first three URSI International Student Paper Prize Competitions at the URSI General Assemblies and Scientific Symposia held in Chicago, Illinois in 2008; Istanbul, Turkey in 2011; and Beijing, China in 2014. Previously, he chaired the Annual USNC-URSI Student Paper Prize Competition at the National Radio Science Meeting in Boulder, CO, USA, each year from 2004–2008 and at the URSI North American Radio Science Meeting in Ottawa, ON, Canada, in 2007. In addition, he has served as Technical Program Co-Chair for the USNC-URSI National Radio Science Meetings held each January in Boulder, CO, USA, from 2010 to 2014. He served as the Secretary of USNC-URSI Commission F (2006–2008) and is a member of URSI Commissions F, G, and H, the American Meteorological Society, the American Geophysical Union, Tau Beta Pi, and Eta Kappa Nu. He was the recipient of the NSF CAREER Award (2003–2008) in the areas of physical and mesoscale dynamic meteorology and the ONR Young Investigator Program Award (2000–2003) for passive microwave remote sensing of the oceans, the Barbara H. and Joseph I. Goldstein Outstanding Junior Faculty Award in 2004, the Lilly Teaching Fellowship for 2001–2002, and a Young Scientist Award at the URSI General Assembly in Toronto, Canada, in 1999. While at Stanford, he received first place in the United States National Committee (USNC) of URSI Student Paper Competition at the 1998 National Radio Science Meeting in Boulder, CO, USA.

Scott M. Ellis, photograph and biography not available at the time of publication.

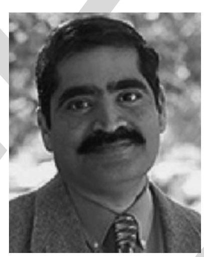

Jothiram Vivekanandan (M'05–SM'10) received the B.E. degree in electronics and communications engineering from the Madurai Kamaraj University, Madurai, India, the M.Tech. degree in microwave and radar engineering from the Indian Institute of Technology, Kharagpur, India, and the Ph.D. degree in electrical engineering from Colorado State University, Fort Collins, CO, USA, in 1986.

He holds a Senior Scientist appointment with both the Earth Observing Laboratory and the Research Applications Laboratory, National Center for Atmospheric Research (NCAR), Boulder, CO, USA. His research interests include the interpretation of remote sensing instruments' responses to clouds and precipitation using mathematical models and actual field observations.

Dr. Vivekanandan is an Associate Editor of *Radio Science*.

Paquita Zuidema is a Professor with the Rosenstiel School of Marine and Atmospheric Science, University of Miami, FL, USA . She was a National Research Council Postdoctoral Fellow with the NOAA Environmental Technology Laboratory, Boulder, CO, USA from 2001 to 2004, an experience that activated an interest in surface-based and in situ microwave radiometry.